Numerical simulation of infrasound propagation in a realistic atmosphere : nonlinear and viscous effects

R. Sabatini[a,b], O. Marsden[a], C. Bailly[a] and O. Gainville[b]

a. LMFA, UMR CNRS 5509 & École Centrale de Lyon, 69134 Écully cedex, France
b. CEA, DAM, DIF, F-91297 Arpajon, France

Résumé

Des simulations numériques directes des équations de Navier-Stokes bidimensionnelles sont effectuées pour déterminer le champ de pression produit par une source infrasonore dans une atmosphère réaliste. L'algorithme numérique repose sur une méthode aux différences finies dans le domaine temporel développée pour des applications en aéroacoustique. La distorsion de la signature acoustique due aux non linéarités ainsi que les effets de dissipation visqueuse sont analysés et discutés.

Abstract

Direct numerical simulations of the two-dimensional compressible Navier-Stokes equations are performed to compute the sound field generated by an infrasonic source in a realistic atmosphere. The numerical algorithm is based on an optimized finite- difference time-domain algorithm developed for aeroacoustic applications. Waveform distortion due to non-linearities as well as viscous dissipation effects are investigated and discussed.

Key words : direct numerical simulation, atmospheric infrasound propagation, nonlinear effects, viscous effects

1 Introduction

Infrasonic waves propagate throughout the Earth's atmosphere along cyclic trajectories which extend up to thermospheric altitudes [1]. A variety of physical phenomena affects the pressure fluctuations recorded at a given distance from the acoustic source. Above all, the exponential reduction with altitude of the mean atmospheric density contributes highly to the development of waveform distortion effects. Non-linearities cause signal steepening, leading first to the harmonic generation associated with shock formation and later to the low frequency production due to period lengthening. Absorption also increases as the mean atmospheric density diminishes, as a consequence of the increase in the mean kinematic viscosity. An interplay between nonlinear and viscous effects is therefore generally observed in the upper atmosphere, where infrasonic signals are refracted back towards the Earth's surface [2, 3].

A correct and complete description of these phenomena relies on the full Navier-Stokes equations. Their accurate resolution is still a challenging task and requires well suited numerical techniques. Recently,

Marsden *et al.* [4] have successfully performed a direct numerical simulation of the Navier-Stokes equations to compute the two-dimensional sound field generated by an infrasonic source in a realistic atmosphere. An analysis of the effect of source strength on signals recorded at ground level was undertaken. To this end, an optimized finite-difference time-domain method originally developed for aeroacoustic applications was used [5, 6, 7]. In this work, the same numerical approach is adopted to investigate the relative importance of nonlinear and viscous effects. Specifically, pressure fluctuations detected on the vertical line above the source up to 180 km altitude are studied. Computations are carried out with different source amplitudes and, in some cases, with a vanishing viscosity, in order to highlight the strong attenuation operated by viscous dissipation.

The paper is organized as follows. The physical problem and numerical algorithm are recalled in Sections 2 and 3. In Section 4, a brief description of the source and the sound field is first provided. The main analysis on the interplay between nonlinear and viscous effects is then performed. Concluding remarks are finally given in Section 5.

2 Problem statement

The propagation of a finite-duration signal emitted by an infrasonic source in a realistic atmosphere extending up to 180 km altitude and 600 km range is simulated. A Cartesian coordinate system Ox_1x_2 with origin at ground level (Figure 1) is used. The acoustic field is analysed in the positive x_1-direction.

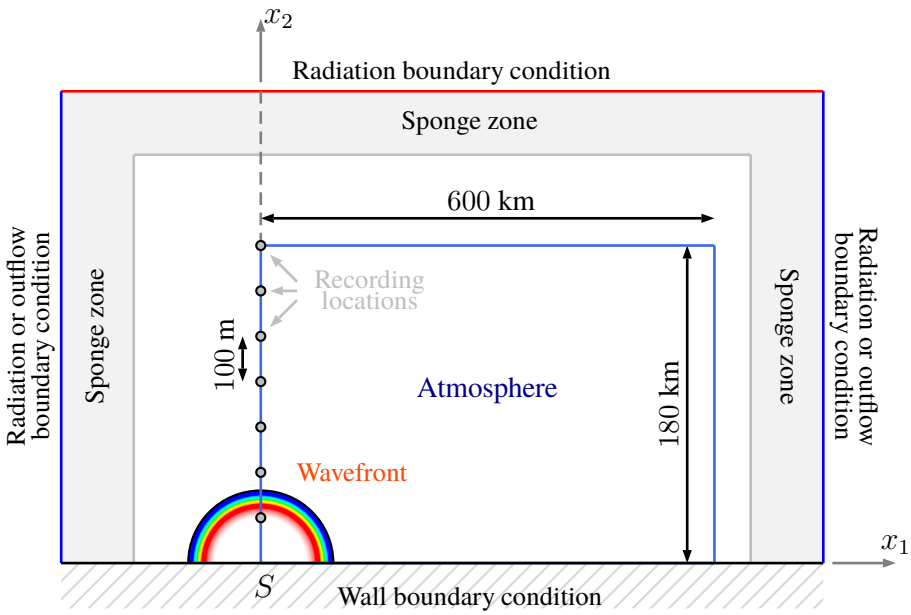

Figure 1: Sketch of the computational domain. The source is located at the point S and the blue rectangle indicates the physical domain.

Sound propagation is governed by the two-dimensional compressible Navier-Stokes equations, which

can be written as

$$\begin{aligned}
&\frac{\partial \rho}{\partial t} + \frac{\partial \left(\rho u_j\right)}{\partial x_j} = 0 \\
&\frac{\partial \left(\rho u_i\right)}{\partial t} + \frac{\partial \left(\rho u_i u_j\right)}{\partial x_j} = -\frac{\partial p}{\partial x_i} + \frac{\partial \tau_{ij}}{\partial x_j} - \rho g \delta_{i2} \\
&\frac{\partial \left(\rho e_t\right)}{\partial t} + \frac{\partial \left(\rho e_t u_j\right)}{\partial x_j} = -\frac{\partial \left(p u_j\right)}{\partial x_j} - \frac{\partial q_j}{\partial x_j} + \frac{\partial \left(u_i \tau_{ij}\right)}{\partial x_j} - \rho g u_2 + \Lambda_s
\end{aligned} \tag{1}$$

where Λ_s represents a source forcing term. The fluid is assumed to be Newtonian, with its viscous stress tensor given by $\tau_{ij} = \mu(\partial u_i/\partial x_j + \partial u_j/\partial x_i - (2/3)\partial u_k/\partial x_k \delta_{ij})$, where μ is the dynamic viscosity computed through the Sutherland's law [8]. Finally, the heat flux is calculated with the Fourier law $q_i = -(\mu c_p/\mathrm{Pr})\,\partial T/\partial x_i$, where Pr is the Prandtl number and c_p the specific heat at constant pressure. Air in the atmosphere is here assumed to behave as an ideal gas, which satisfies the equation of state $p = \rho r T$, where r is the specific gas constant. The numerical values of the various constants can be found in Marsden *et al.* [4].

The Earth's surface is modelled as a perfectly reflecting flat wall. The infrasonic source Λ_s is placed at the origin of the domain $S = (0\,\mathrm{km}, 0\,\mathrm{km})$ and computed as

$$\Lambda_s\left(x_1, x_2, t\right) = \frac{\mathcal{A}_s}{2} \begin{cases} \sin\left(\omega_s t\right)\left[1 - \cos\left(\omega_s t\right)\right] e^{-\log(2)\left(x_1^2 + x_2^2\right)/b_s^2} & t \in [0, T_s] \\ 0 & \text{otherwise} \end{cases} \tag{2}$$

where $\mathcal{A}_s$ is the amplitude, b_s the half-width and f_s the frequency. In this work, b_s is set to 600 m and $f_s = \omega_s/(2\pi) = 1/T_s$ to 0.1 Hz, so that the total emission duration is of $T_s = 10$ seconds.

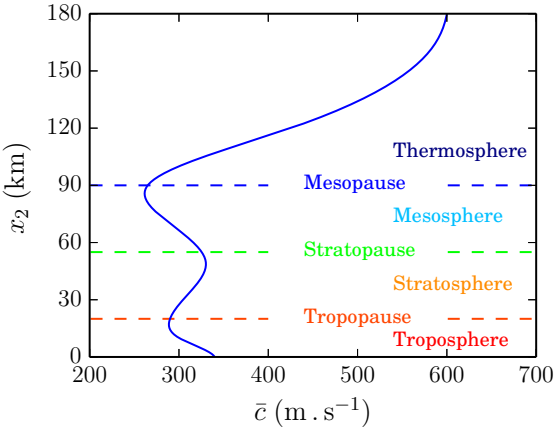

Figure 2: Sound speed profile

The mean atmosphere is modelled as a vertically stratified medium, $\bar{\rho} = \bar{\rho}(x_2)$, $\bar{u}_1 = \bar{u}_1(x_2)$, $\bar{u}_2 \equiv 0$ and $\bar{\rho}\bar{e}_t = \bar{\rho}(x_2)\bar{e}_t(x_2)$. It is constructed from a spline-based speed of sound profile, which reproduces the large scales observed during the *Misty Picture experiment* [2] from 0 km to around 180 km (Figure 2). Spline knot locations and values are taken from a previous study [9]. The mean temperature is computed according to the expression $\bar{T}(x_2) = \bar{c}(x_2)^2/(\gamma r)$, whereas the pressure profile is obtained by solving the hydrostatic equilibrium equation $d\bar{p}/dx_2 = -g\bar{p}(r\bar{T})$. Finally, the density profile is determined from the equation of state $\bar{\rho} = \bar{p}/(r\bar{T})$.

Simulations are carried out for source amplitudes $\mathcal{A}_s$ ranging from 10^{-1} J.m^{-3}.s^{-1} to 10^{+3} J.m^{-3}.s^{-1}. Pressure fluctuations are recorded on the x_2-axis every 100 m up to 180 km.

3 Numerical approach

System (1) is solved on a regular Cartesian grid with an optimized finite-difference time-domain algorithm developed for aeroacoustic simulations [5, 6, 7]. Spatial discretization is performed with an explicit fourth-order 11-point centered scheme which has been built up to reduce dispersion on wavelengths larger than about five grid spacings. Time integration is carried out with a six-step second-order low-storage Runge-Kutta algorithm. An explicit fourth-order 11-point stencil spatial low-pass filter is applied to ensure stable computations. Additionally, a shock-capturing procedure is employed to handle acoustic shocks which are generated during propagation.

An isotropic grid with a spacing of $\Delta = \Delta x_1 = \Delta x_2 = 100$ m is used. The whole computational domain contains $7168 \times 2560 \sim 20$ million points. As a result of the large values of the kinematic viscosity in the upper atmosphere, the time step Δt is constrained by the maximum allowed Fourier number $\mathrm{Fo} = \bar{\nu}_u \Delta t / \Delta x^2$, where the subscript u indicates the *upper* boundary of the physical domain, $x_2 = 180$ km. In this work, a value of $\mathrm{Fo} = 0.3$ is chosen, so that $\Delta t \simeq 0.034$ and $\mathrm{CFL} = \bar{c}_u \Delta t / \Delta \simeq 0.21$.

The numerical algorithm is implemented in the OpenCL environment and executed on a AMD Radeon R9 200 Series GPU (Graphics Processing Unit) with a memory allocation limit of 4 GB.

4 Results

4.1 Source characterization

The signal resulting from the infrasonic source is illustrated in Figure 3, which presents pressure fluctuations recorded at the origin of the domain for $\mathcal{A}_s = 10^{-1}$ J.m^{-3}.s^{-1}, along with the corresponding one-sided energy spectral density. The maximum overpressure P_s detected at the point S is of about 0.024 Pa and the frequency f_p of the maximum ESD is around 0.11 Hz. The waveform at the source location is found to be independent from the parameter $\mathcal{A}_s$, at least for amplitudes up to 10^4 J.m^{-3}.s^{-1}, and the value of P_s scales approximately as $\mathcal{A}_s/4$.

The one-sided energy spectral density of the signal recorded on the x_2-axis at $x_2 = 1$ km, $A = (0\,\mathrm{km}, 5\,\mathrm{km})$, is also reported in orange for comparison. A slight shift of the frequency f_p of the maximum ESD towards a lower value is observed as a results of the non compactness of the source, whose Helmholtz number $\mathrm{He} = k_s b_s = 2\pi f_s b_s / \bar{c}(0)$ is around 1.1. The Gaussian source distribution acts as a low-pass filter on the signal emitted.

4.2 Brief description of the sound field

As a result of the atmospheric stratification, the amplitude of pressure fluctuations is expected to be proportional to the square root of the mean density [10]. The following normalized pressure variable is thus defined

$$\Phi(x_1, x_2, t) = \frac{p(x_1, x_2, t) - \bar{p}(x_2)}{\mathcal{A}_s \sqrt{\bar{\rho}(x_2)}} \tag{3}$$

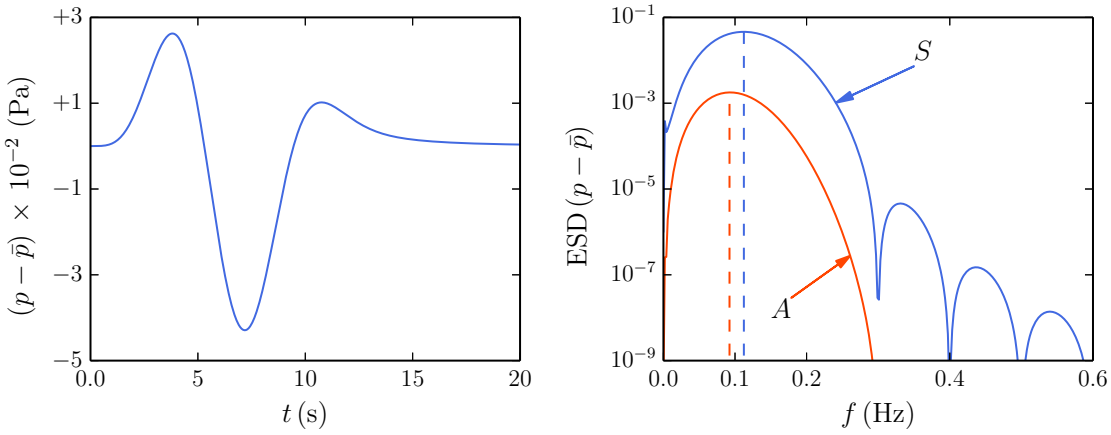

(a) (b)

Figure 3: (a) Fluctuating pressure recorded at the source location for $\mathcal{A}_s = 10^{-1}$ J.m^{-3}.s^{-1}. (b) One-sided energy spectral density at points S and A.

The parameter $\mathcal{A}_s$ is here introduced to allow comparisons for different source amplitudes. Some snapshots of the acoustic field Φ obtained for $\mathcal{A}_s = 10^{-1}$ J.m^{-3}.s^{-1} are displayed in Figure 4 for different time instants. Acoustic rays are also superimposed. Owing to the mean sound speed profile, acoustic waves are continuously refracted while propagating through the atmosphere. Consequently, the wavefront released by the infrasonic source rapidly loses its initially isotropic shape (Figure 4(a)). Between $t = 1.4 \times 10^4\,\Delta t$ and $t = 2.0 \times 10^4\,\Delta t$ a cusp caustic appears at about 110 km altitude (Figures 4(b) and 4(c)). The acoustic rays which have reached the upper atmospheric layers turn now towards the Earth's surface. A waveguide is thus created between the land and the lower thermosphere. These thermospheric waves become audible at the ground at about 250 km (Figure 4(d)). For simulation times larger than $2.7 \times 10^4\,\Delta t$, the sound field becomes more and more complex and a multitude of arrivals reaches the Earth's surface. Along with the thermospheric signals, arch-like wavefronts are generated by diffraction in the waveguide (Figure 4(e)). Between about $x_1 = 250$ km and $x_1 = 500$, the thermospheric rays are reflected by the ground (Figure 4(e)). A new cusp caustic thus appears at 110 km altitude. The subsequent thermospheric signals are finally seen to arrive at ground level at about 550 km away from the source (Figure 4(f)).

4.3 Nonlinear and viscous effects

The one-sided energy spectral density computed along the x_2-axis for $\mathcal{A}_s = 10^{-1}$ J.m^{-3}.s^{-1} is shown in Figure 5. As a consequence of the weak source amplitude, the signal Φ undergoes negligible distortion during its vertical propagation up to about 120 km. Outside the source region and below $x_2 \leq 100$ km, the frequency of the maximum ESD remains essentially constant at the value $f_p \simeq 0.093$ Hz and the amplitude of the pressure fluctuations decreases because of the 2D cylindrical spreading. This result is confirmed in Figure 5(b), where the one-sided energy spectral density associated with the source frequency f_s is compared to the approximate solution of the variable index Helmholtz equation

$$\mathrm{ESD}_{\mathrm{He}}\left(\Phi\right) \sim \left|\mathcal{H}_0^{(1)}\left(\omega x_2/\bar{c}\right)\right|^2$$

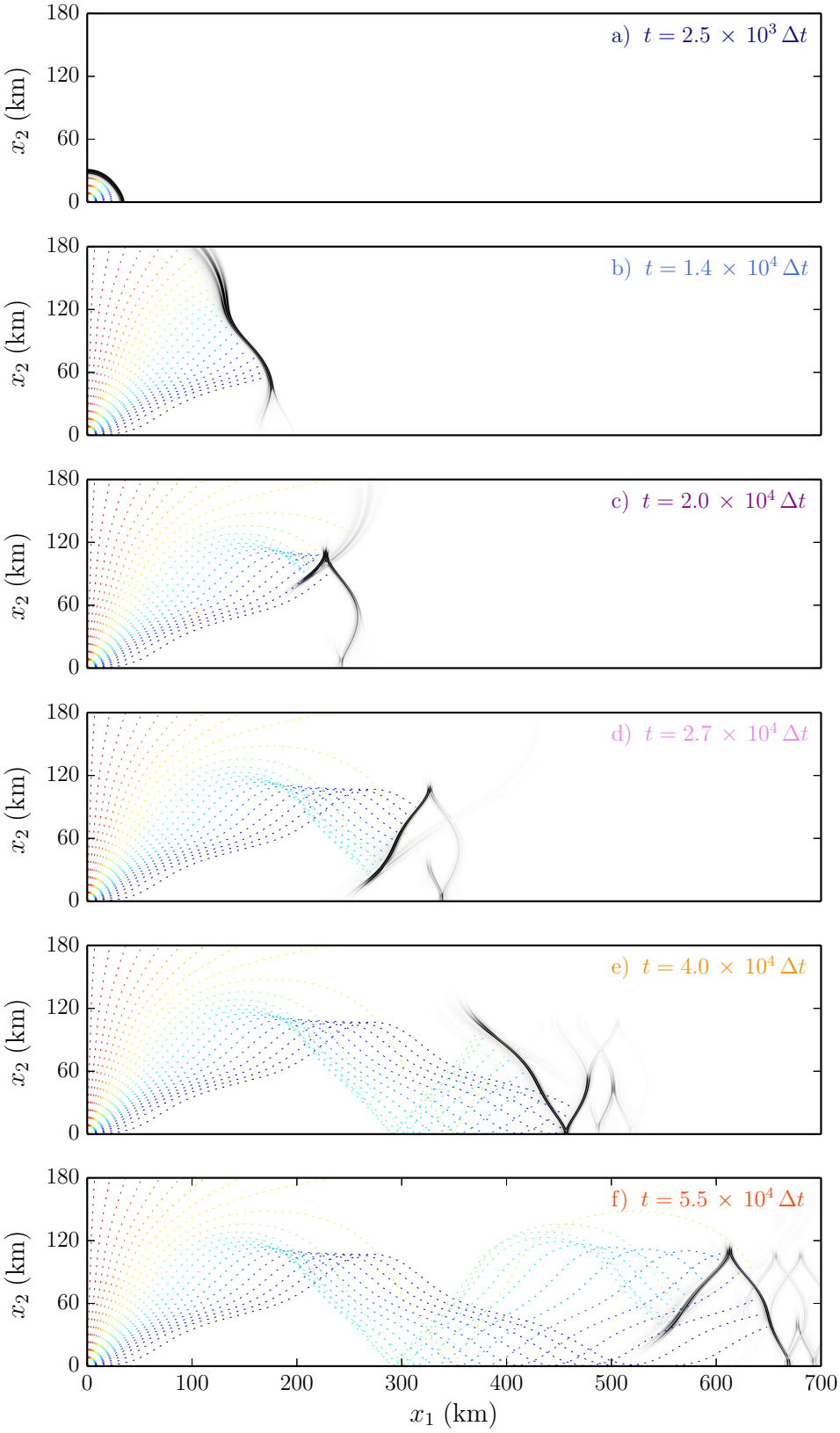

Figure 4: Snapshots of the normalized pressure variable Φ at different time instants. A ray tracing is also superimposed in dashed color lines to improve the readability.

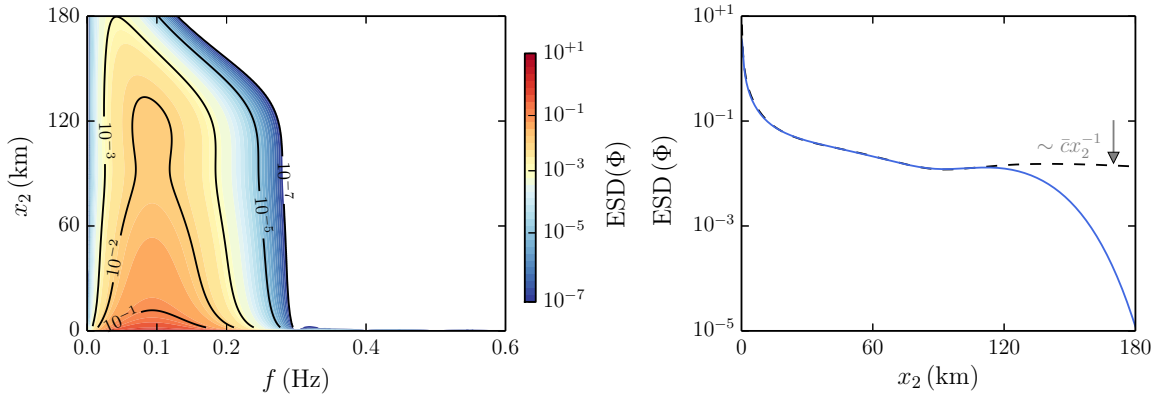

(a) (b) Cross-sectional view for $f = f_s$

Figure 5: (a) ESD of the whole signal recorded along the x_2-axis and above the source. (b) ESD profile for $f = f_s$ in blue solid line, and approximate analytical solution in black dashed line.

with $\mathcal{H}_0^{(1)}$ the zeroth-order Hankel function of the first kind. The agreement is remarkably good up to 120 km of height. For higher altitudes, viscous dissipation becomes more and more important due to the exponential diminution of the mean density. The kinematic viscosity $\bar{\nu}$ increases by about 10 orders of magnitude between the ground and 180 km altitude. Consequently, the signal amplitude drops down and a shift towards lower frequencies is observed, since absorption phenomena depend not only on the diffusion parameter $\bar{\nu}$ but also on the square of the frequency.

For larger source amplitudes, nonlinear effects become predominant and the initial smooth signal is distorted during the vertical propagation. At a characteristic distance x_2^{shock} from the source, and for high enough values of the source amplitude $\mathcal{A}_s$, shock waves are generated. Some signals recorded on the x_2-axis for $\mathcal{A}_s = 10^{+4}$ J.m^{-3}.s^{-1} are shown in Figure 6. At $x_2 = 25$ km, the normalized pressure

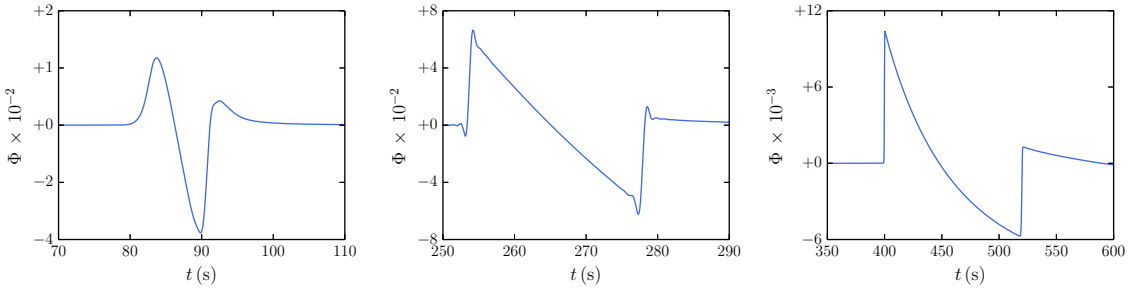

(a) $x_2 = 25$ km (b) $x_2 = 80$ km (c) $x_2 = 150$ km

Figure 6: Signals recorded at different altitudes for $\mathcal{A}_s = 10^{+4}$ J.m^{-3}.s^{-1}

fluctuation Φ is still a smooth function but its waveform has undergone appreciable modifications (Figure 6(a)). Besides, its amplitude has diminished by a factor 10 as a consequence of the 2D cylindrical spreading. The waveform steepens with increasing time and distance and evolves into an N-shaped wave (Figure 6(b)). Once the N-wave is formed, it lengthens while propagating towards the upper atmosphere. Its duration is about three source periods at $x_2 = 80$ km and greater than $10T_s$ at $x_2 = 150$ km. Moreover, due to the very large signal amplitude, its waveform does not remain self-similar. At $x_2 = 150$ km, a curved central part is observed (Figure 6(c)).

The one-sided energy spectral density of the normalized fluctuating pressure Φ recorded along the vertical x_2 axis for $\mathcal{A}_s = 10^{+4}$ J.m^{-3}.s^{-1} is shown in Figure 7(a). The shock formation coincides with a

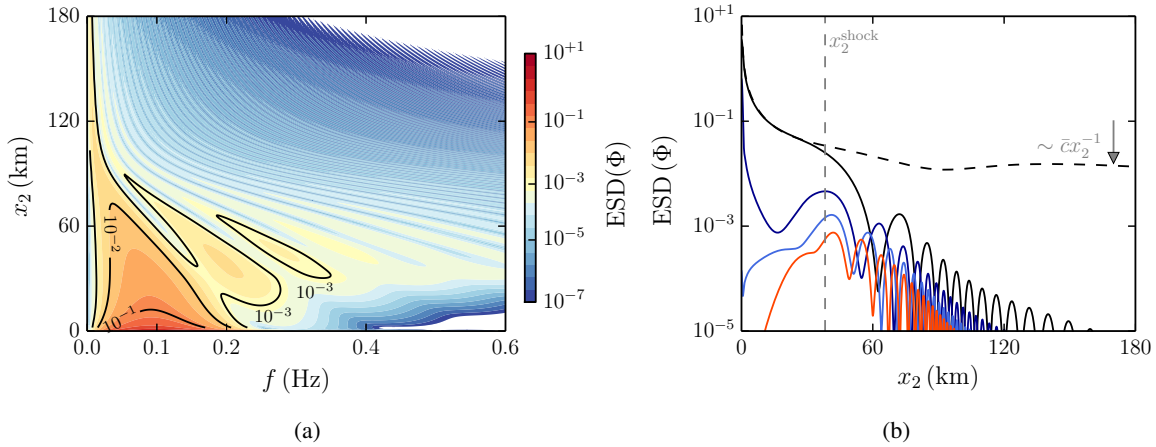

(a) (b)

Figure 7: (a) ESD of the signals recorded on the x_2-axis above the source in the nonlinear regime. (b) Cross-sectional view for $f = f_s$ (black line), $f = 2f_s$ (dark blue line), $f = 3f_s$ (blue line) and $f = 4f_s$ (orange line).

sharp enlargement of the spectrum. For distances from the source smaller than $x_2 \simeq 10$ km, most of the energy is found at the source frequency f_s, whereas, above $x_2 \simeq 10$ km, the energy of higher harmonics becomes significant. The behaviour of the ESD as a function of the altitude is shown in Figure 7(b) for four different spectral component frequencies, $f = nf_s$ with $n = 1, \ldots, 4$. As the shock formation implies a transfer of energy towards shorter waves, the energy associated with the fundamental frequency drops with height, whereas the ESD of the harmonics rapidly increases and reaches a maximum value around $x_2 = 40$ km. For altitudes above x_2^{shock}, the lengthening of the N-wave causes an energy shift towards lower frequencies. Therefore, the shock formation distance x_2^{shock} can be computed here as the distance x_2 from the source at which the ESD of the first harmonic reaches its maximum value. For $\mathcal{A}_s = 10^{+4}$ J.m^{-3}.s^{-1}, it is observed that $x_2^{\text{shock}} = 38.2$ km. For this source amplitude, viscous effects are found to play a minor role on the acoustic signature. When the wavefront reaches the thermosphere, where they are expected to become important, most of the signal energy is contained in frequencies which are too low for absorption phenomena to be significant. More specifically, even though the kinematic viscosity grows exponentially with altitude, attenuation is insignificant as a result of the short propagation distance.

The shock formation distance x_2^{shock} is plotted in Figure 8 as a function of the peak overpressure P_s at the source location. As expected, x_2^{shock} diminishes as P_s increases. It is worth noting that the decrease of the mean density contributes highly to the generation of N-waves, and more generally, to the development of nonlinear effects. Following Crocker [12], an estimate of the shock formation distance for harmonic cylindrical waves in a homogeneous medium can be obtained through the formula $x_2^{\text{shock}} \simeq r_0 \left[1 + \bar{\rho}\bar{c}^3/(4\pi\beta P_0 f_0 r_0)\right]^2$, which is valid in the weakly-nonlinear regime. Here, r_0 is the radius of the initial wavefront, P_0 and f_0 the corresponding overpressure and frequency, and $\beta = (\gamma + 1)/2$. Taking $r_0 = 10$ km and $f_0 = 0.1$ Hz, and considering that the overpressure at $x_2 = r_0$ obtained for $P_s \simeq 2595.4$ Pa is $P_0 \simeq 410$ Pa, x_2^{shock} would be of order 700 km, if calculated with the ground conditions $\bar{\rho}(0\,\text{km}) = 1.2111$ kg.m^{-3} and $\bar{c}(0\,\text{km}) = 340$ m.s^{-1}.

The frequency f_p of the maximum ESD is plotted in Figure 9 as a function of the altitude x_2 for different

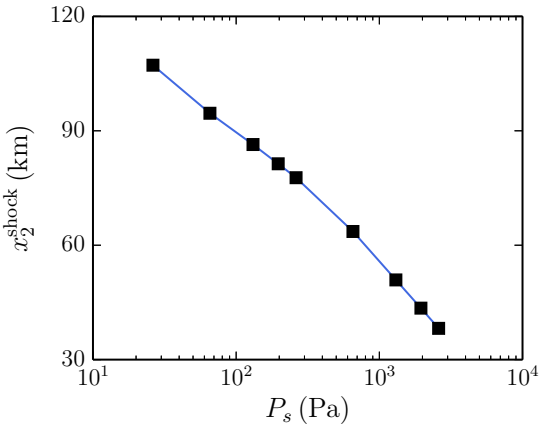

Figure 8: Shock formation distance as a function of the source peak overpressure

source amplitudes. In all cases a shift towards lower frequencies is observed. For $\mathcal{A}_s = 10^{-1}$ J.m^{-3}.s^{-1}, nonlinear effects are negligible and the shift is only attributed to viscous dissipation, whereas for $\mathcal{A}_s = 10^{+4}$ J.m^{-3}.s^{-1}, it is induced by the lengthening of the N-wave. For intermediate source amplitudes, both nonlinear and absorption phenomena are involved. Finally, the frequency f_p of the N-wave is expected to vary asymptotically as $\sim 1/(3\tau^+)$, where τ^+ represents the duration of the positive phase [11, 13], and this result is observed by the numerical simulations for values of $\mathcal{A}_s$ higher than about 10^{+2} J.m^{-3}.s^{-1}.

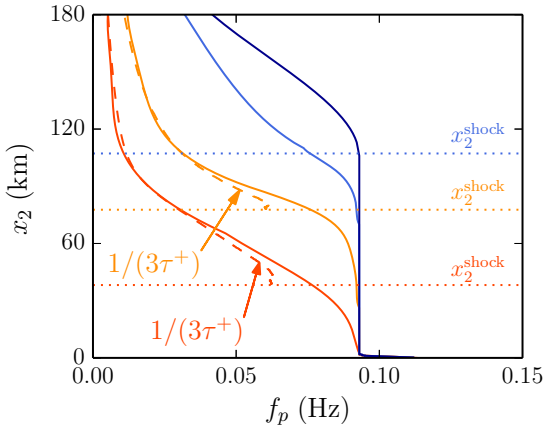

Figure 9: Maximum frequency for different source peak overpressures: $\mathcal{A}_s = 10^{-1}$ J.m^{-3}.s^{-1}, $\mathcal{A}_s = 10^{+2}$ J.m^{-3}.s^{-1}, $\mathcal{A}_s = 10^{+3}$ J.m^{-3}.s^{-1} and $\mathcal{A}_s = 10^{+4}$ J.m^{-3}.s^{-1}.

Nonlinear effects are found to be appreciable for source amplitudes higher than 10^{+1} J.m^{-3}.s^{-1}. However, shock formation is only observed for values of $\mathcal{A}_s$ greater than about 10^{+2} J.m^{-3}.s^{-1}, refer to Figure 8. For intermediate values, the Euler equations predict nonlinear steepening, but viscous effects actually prevent shock formation or rapidly erase all the discontinuities. For larger $\mathcal{A}_s$, dissipation of harmonics tends to attenuate the peak overpressure. As an example, signals recorded at $x_2 = 110$ km and $x_2 = 170$ km for $\mathcal{A}_s = 2.5 \times 10^2$ J.m^{-3}.s^{-1}, and computed with and without viscous terms are illustrated in Figure 10. At $x_2 = 110$ km, an N-wave is observed. Up to this altitude, absorption plays a minor role. The two curves are practically superimposed. On the contrary, a remarkable departure

from the Euler model is seen at $x_2 = 170$ km. In the propagation through the thermosphere, viscous dissipation strongly attenuates the signal. The maximum overpressure is almost halved if compared with the value obtained without viscosity. The central part of the wave and the frequency f_p remain however untouched.

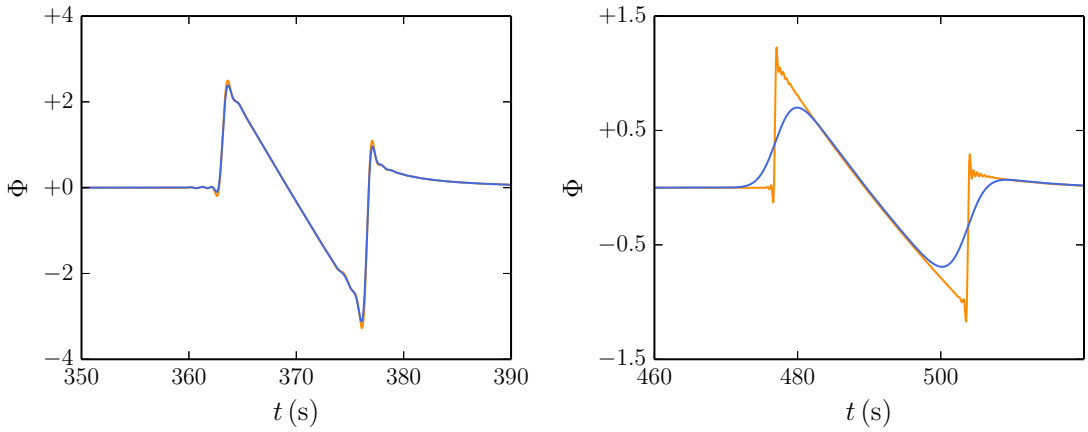

(a) $x_2 = 110$ km (b) $x_2 = 170$ km

Figure 10: Signals recorded at two different altitudes and computed for $P_s = 65.6$ Pa with (———) and without (———) viscous absorption.

Attenuation in the upper atmosphere obviously reduces with increasing source amplitude. Shock formation occurs at lower and lower altitudes and the energy of the signal arriving in the thermosphere is contained in lower and lower frequencies, due to the lengthening of the N-wave. In order to get more insight into the evaluation of the importance of viscous effects, the following altitude-dependent acoustic Reynolds number, based on the mean speed of sound, is introduced

$$\mathrm{Re}_a = \frac{(\bar{c}/\bar{f})\bar{c}}{\bar{\nu}}$$

where $\bar{f}$ is a characteristic frequency of the signal. For a given altitude, this characteristic frequency can be defined as

$$\bar{f}(x_2) = \frac{\displaystyle\int_0^\infty f \left|\hat{\Phi}(0, x_2, f)\right|^4 df}{\displaystyle\int_0^\infty \left|\hat{\Phi}(0, x_2, f)\right|^4 df}$$

where $\hat{\Phi}$ is the Fourier transform of the normalized pressure Φ. The corresponding acoustic Reynolds number is plotted in Figure 11 for different source peak overpressures.

As already highlighted, for the source frequency and amplitudes considered in this study, absorption effects become important during the propagation in the thermosphere. They have a noticeable influence on the acoustic signature for source amplitudes lower than about 5×10^2 J.m^{-3}.s^{-1}. In these cases, the acoustic Reynolds number is smaller than 10^3 above say 120 km altitude. For higher values of Re_a, significant attenuation cannot be observed below 180 km altitude and the signal would have to propagate over far larger distances to detect viscous effects.

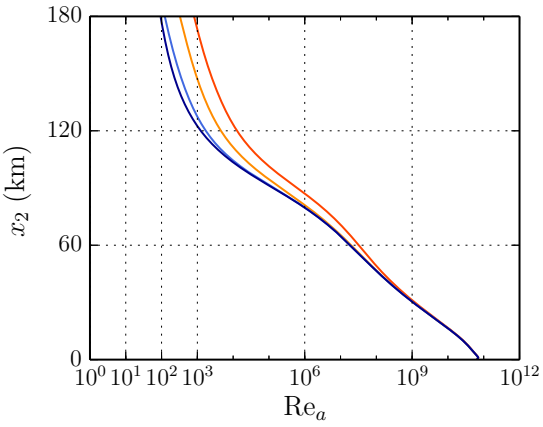

Figure 11: Acoustic Reynolds number for different source peak overpressures: $\mathcal{A}_s = 10^{-1}$ J.m^{-3}.s^{-1}, $\mathcal{A}_s = 10^{+2}$ J.m^{-3}.s^{-1}, $\mathcal{A}_s = 10^{+3}$ J.m^{-3}.s^{-1} and $\mathcal{A}_s = 10^{+4}$ J.m^{-3}.s^{-1}.

5 Conclusion

Direct numerical simulations of the full two-dimensional Navier-Stokes equations are performed to investigate the relative importance of nonlinear and viscous effects in atmospheric infrasound propagation. For the source frequency considered in this work, attenuation is found to play an important role in the upper atmosphere for small and moderate amplitudes. For intermediate values of the source strength, absorption of harmonics may even prevent shock formation or rapidly erase discontinuities. On the contrary, in strongly nonlinear cases, the characteristic diffusion length becomes far larger than the propagation distances of interest, and viscous dissipation only marginally affects the acoustic signature.

6 Acknowledgements

The first author thanks the Direction Générale de l'Armement (DGA) for the financial support. Present results have been obtained within the frame of LETMA (Laboratoire ÉTudes et Modélisation Acoustique), Contractual Research Laboratory between CEA, CNRS, École Centrale de Lyon, C-Innov and Université Pierre et Marie Curie.

References

[1] S.N. Kulichkov, I.P. Chunchuzov, G.A. Bush, and V.G. Perepelkin. Physical modeling of long-range infrasonic propagation in the atmosphere. *Izvestiya, Atmospheric and Oceanic Physics*, **44**(2), 175–186, (2008).

[2] O Gainville, Ph Blanc-Benon, E Blanc, R Roche, C Millet, F Le Piver, B Despres, and PF Piserchia. Misty picture: a unique experiment for the interpretation of the infrasound propagation from large explosive sources. In *Infrasound Monitoring for Atmospheric Studies*, p. 575–598. (Springer Netherlands, 2009).

[3] J.B. Lonzaga, R.M. Waxler, J.D. Assink and C.L. Talmadge. Modelling waveforms of infrasound arrivals from impulsive sources using weakly non-linear ray theory. *Geophys. J. Int.*, **200**(3), 1347–1361, (2015).

[4] O. Marsden, C. Bogey, and C. Bailly. A study of infrasound propagation based on high-order finite difference solutions of the Navier-Stokes equations. *J. Acoust. Soc. Am.*, **135**(3), (2014).

[5] C. Bogey and C. Bailly. A family of low dispersive and low dissipative explicit schemes for noise computations. *J. Comput. Phys.*, **194**(1), 194–214, (2004).

[6] J. Berland, C. Bogey, O. Marsden, and C. Bailly. High-order, low dispersive and low dissipative explicit schemes for multiple-scale and boundary problems. *J. Comput. Phys.*, **224**, 637–662, (2007).

[7] C. Bogey, N. De Cacqueray, and C. Bailly. A shock-capturing methodology based on adaptive spatial filtering for high-order non-linear computations. *J. Comput. Phys.*, **228** 1447–1465, (2008).

[8] L. C. Sutherland and H. E. Bass. Atmospheric absorption in the atmosphere up to 160 km. *J. Acoust. Soc. Am.*, **115**(3), 1012–1032, (2004). See also Erratum. J. Acoust. Soc. Am., **120**(5), 2985 (2006).

[9] O. Marsden and O. Gainville. Nonlinear effects in infrasound propagation simulations. *Acoustics 2012 Nantes*, (2012).

[10] P.G. Bergmann. The wave equation in a medium with a variable index of refraction. *J. Acoust. Soc. Am.*, **17**(4), 329–333, (1946).

[11] P.H. Rogers and J.H. Gardner. Propagation of sonic booms in the thermosphere. *J. Acoust. Soc. Am.*, **67**(1), (1980).

[12] M.J. Crocker. Handbook of Acoustics. John Wiley & Sons, Inc., (1998).

[13] S.N. Kulichkov. Evidence for Nonlinear Atmospheric Effects in Infrasound Propagation from Explosions of Different Types and Yields. *Nonlinear Acoustics - Fundamentals and Applications: 18th International Symposium on Nonlinear Acoustics - ISNA 18*, (2008).